

1 **Broadband spectral responses in visual cortex revealed by a new**
2 **MEG denoising algorithm**

3
4 Eline R. Kupers¹, Helena X. Wang¹, Kaoru Amano², Kendrick N. Kay³, David J. Heeger¹,
5 Jonathan Winawer¹

6 **Author institutions**

- 7 1. Department of Psychology and Center for Neural Science, New York University, New
8 York, NY 10003
9 2. Center for Information and Neural Networks (CiNet), National Institute of Information and
10 Communications Technology, Osaka 565-0871
11 3. Center for Magnetic Resonance Research, University of Minnesota, Minneapolis, MN
12 55414

13
14 **Short title:** Broadband spectral responses in visual cortex

15
16 **Contact information:**

17 Eline Kupers
18 Department of Psychology, New York University
19 New York University
20 6 Washington Place, Room 959
21 New York, NY 10003
22 eline.kupers@nyu.edu

23
24 **Number of words**

25 Abstract: 236
26 Introduction: 645
27 Discussion: 1647

28
29 **Conflict of Interest:** The authors declare no competing financial interests

30
31 **Acknowledgments:**

32 This study was supported NEI grant R00-EY022116 (J.W.), and NIMH grant R01-MH111417
33 (J.W.).

34 Abstract

35 Currently, non-invasive methods for studying the human brain do not reliably measure spike-rate-
36 dependent signals, independent of other responses such as hemodynamic coupling (fMRI) and
37 subthreshold neuronal synchrony (oscillations and event-related potentials). In contrast, invasive
38 methods – animal microelectrode recordings and human electrocorticography (ECoG) – have
39 recently measured broadband power elevation in field potentials (~50-200Hz) as a proxy for the
40 locally averaged spike rates. Here, we sought to detect and quantify stimulus-related broadband
41 responses using magnetoencephalography (MEG) in individual subjects. Because extracranial
42 measurements like MEG have multiple global noise sources and a relatively low signal-to-noise
43 ratio, we developed an automated denoising technique, adapted from ([Kay et al., 2013](#)), that helps
44 reveal the broadband signal of interest. Subjects viewed 12-Hz contrast-reversing patterns in the
45 left, right, or bilateral visual field. Sensor time series were separated into an evoked component
46 (12-Hz amplitude) and a broadband component (60–150Hz, excluding stimulus harmonics). In all
47 subjects, denoised broadband responses were reliably measured in sensors over occipital cortex.
48 The spatial pattern of the broadband measure depended on the stimulus, with greater broadband
49 power in sensors contralateral to the stimulus. Because we obtain reliable broadband estimates
50 with relatively short experiments (~20 minutes), with a sufficient signal-to-noise-ratio to
51 distinguish responses to different stimuli, we conclude that MEG broadband signals, denoised with
52 our method, offer a practical, non-invasive means for characterizing spike-rate-dependent neural
53 activity for a wide range of scientific questions about human brain function.

54 Significance Statement

55 Neuronal activity causes perturbations in nearby electrical fields. These perturbations can be
56 measured non-invasively in the living human brain using EEG and MEG. These techniques have
57 emphasized two kinds of measurements: oscillations and event-related responses. A third type of
58 signal, a stimulus-related increase in power spanning a wide range of frequencies ('broadband'), is
59 routinely measured in invasive recordings, but not with MEG and EEG. This broadband response is
60 of great interest because unlike oscillations and event-related responses, it is correlated with
61 neuronal spike rates. Here we report quantitative, spatially specific measurements of broadband
62 fields in individual human subjects using MEG. These results demonstrate that a spike-rate-
63 dependent measure of brain activity can be obtained non-invasively from the living human brain.

64
65 **Key words:** MEG, spectral analysis, denoising, broadband, visual cortex, steady state visual evoked
66 fields

67 Introduction

68 The time-varying electric and magnetic fields near neural tissue provide an indirect but rich source
69 of information about the activity of neural populations ([reviewed by Buzsaki et al., 2012](#)). These
70 signals include rapid, ‘evoked’ responses that are time-locked to stimulus events ([Norcia et al.,
71 2015](#)), oscillatory responses ([Berger, 1929](#)), and non-oscillatory, broadband signals ([Miller et al.,
72 2007](#); [Miller et al., 2009c](#)). Broadband signals associated with sensory or motor tasks have been
73 widely observed in human electrocorticography, or ‘ECoG’, ([Miller et al., 2014](#)) and animal
74 microelectrode recordings ([Henrie and Shapley, 2005](#)). The broadband signal is an elevation in
75 spectral power, typically spanning 50 to >200Hz ([Miller et al., 2009b](#)), and has attracted a great
76 deal of attention for several reasons.

77 First, the broadband signal is correlated with the level of neural activity (multi-unit spiking), and
78 hence provides a way to study population-level spiking activity in a cortical region ([Liu and
79 Newsome, 2006](#); [Manning et al., 2009](#); [Ray and Maunsell, 2011](#)). Second, the broadband signal has a
80 smaller point spread function on the cortical surface than low frequency oscillations (8-25Hz)
81 ([Miller et al., 2009c](#); [Hermes et al., 2012a](#)), and is therefore useful both for characterizing local
82 properties of cortex and as a tool for neural prosthetics ([Schalk and Leuthardt, 2011](#)). Third, the
83 broadband signal is correlated with a portion of the fMRI response and, together with other field
84 potential measures, can be used to understand neural factors underlying an observed BOLD
85 response ([Hermes et al., 2012a](#); [Lima et al., 2014](#)). Finally, because it can be measured at high
86 temporal resolution, the broadband signal is useful for characterizing the temporal dynamics of
87 neuronal activity ([Honey et al., 2012](#); [Podvalny et al., 2017](#)).

88 In contrast to intracranial recordings, in the extracranial measures of electroencephalography
89 (EEG) and magnetoencephalography (MEG), broadband responses have not been widely and
90 reliably observed. One significant challenge in identifying broadband in extracranial measures is
91 that non-neural noise sources, particularly from miniature saccades, can be confounded with
92 experimental designs, making neurally induced broadband responses hard to isolate ([Yuval-
93 Greenberg et al., 2008](#); [Yuval-Greenberg and Deouell, 2009, 2011](#); [Carl et al., 2012](#)).

94 A second challenge in measuring broadband extracranially is that the response is most evident in
95 high frequencies (> 60Hz), and the signal amplitude at these frequencies is low. While intracranial
96 recordings have relatively high signal-to-noise ratios (SNR) even at these higher frequencies ([Miller
97 et al., 2014](#)), EEG and MEG do not ([Hämäläinen et al., 1993](#)). Broadband signals can extend to lower
98 frequencies ([Harvey et al., 2013](#); [Winawer et al., 2013](#)), but oscillatory processes in lower frequency
99 bands often mask broadband measures in this range ([Miller et al., 2009c](#)).

100 A third challenge is the potential confound between broadband signals and narrowband gamma
101 oscillations. Narrowband gamma oscillations have been successfully measured with MEG and EEG,
102 particularly in visual cortex for high contrast gratings ([Hoogenboom et al., 2006](#); [Fries et al., 2008](#);
103 [Muthukumaraswamy and Singh, 2013](#)). The frequency range of these oscillations (30-100Hz)
104 overlaps the broadband range, but the narrowband and broadband signals reflect biologically
105 different processes ([Henrie and Shapley, 2005](#); [Miller et al., 2009b](#); [Ray and Maunsell, 2011](#); [Miller
106 et al., 2014](#)). The ability to measure one does not imply the ability to measure the other.

107 Here, we sought to measure broadband signals quantitatively in the human brain using a non-
108 invasive method (MEG). In order for this important, spike-dependent signal to be useful, it is
109 necessary to measure it reliably in individual subjects, with a high SNR. A high SNR is essential if
110 this signal will be widely used to study differences across stimuli, tasks, or groups. We developed a
111 novel, automated MEG denoising algorithm adapted from prior fMRI work ([Kay et al., 2013](#)). Our
112 experiments were designed to elicit spatially localized neural responses in visual cortex, and eye

113 movements were measured in a subset of subjects to test for possible confounds from non-neural
114 sources.

115 **Methods**

116 **Data acquisition**

117 **Subjects**

118 Eight subjects (five females), ages 20-42 years (M = 28.4 / SD = 6.7 years) with normal or
119 corrected-to-normal vision participated in the NYU study. An additional 4 subjects (M = 27.0 / SD =
120 7.4 years) participated in the same experiment at Center for Information and Neural Networks
121 (CiNet), National Institute of Information and Communications Technology (NICT) in Osaka, Japan.
122 Subjects provided written informed consent. The experimental protocol was in compliance with the
123 safety guidelines for MEG research and was approved by the University Committee on Activities
124 involving Human Subjects at New York University and by the ethics committee of the National
125 Institute of Information and Communications Technology (NICT).

126 **Display**

127 Stimuli were generated using MATLAB (MathWorks, MA) and PsychToolbox ([Brainard, 1997](#); [Pelli,](#)
128 [1997](#)) on a Macintosh computer. NYU: Images were presented using an InFocus LP850 projector
129 (Texas Instruments, Warren, NJ) with a resolution of 1024 x 768 pixels and refresh rate of 60Hz.
130 Images were projected via a mirror onto a front-projection translucent screen at a distance of
131 approximately 42 cm from the subject's eyes (field of view: 22 deg × 22 deg). The display was
132 calibrated with the use of a LS-100 luminance meter (Konica Minolta, Singapore) and gamma-
133 corrected using a linearized lookup table. CiNet: The display parameters were similar, except that
134 the projector was PT-DZ680 (Panasonic, Japan), with 800 x 600 resolution and 60Hz, and 61 cm
135 viewing distance.

136 **Stimuli**

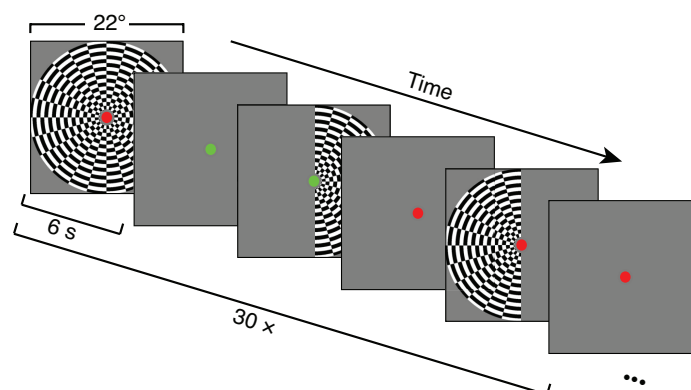
137 The stimuli were contrast-reversing dartboard patterns (12 square wave contrast reversals per
138 second), windowed within either a half circle (left or right visual field) or full circle (bilateral visual
139 field) aperture, with a diameter of 22 degrees at NYU (26 degrees at CiNet). Mean luminance gray
140 (206 cd/m^2 (NYU), 83 cd/m^2 (CiNet)) was used as background color for the dartboards and was
141 shown in the full field during blank trials between stimulus periods (Figure 1).

142 **Experimental design**

143 One *run* consisted of six seconds flickering 'on' periods, alternated with six seconds 'off' mean
144 luminance periods, repeated 6 times (72 seconds). The order of the left-, right- or both-visual field
145 apertures was random. There was a fixation dot in the middle of the screen throughout the run,
146 switching between red and green at random intervals (averaging 3 seconds). The subjects were
147 instructed to maintain fixation throughout the run and press a button every time the fixation dot
148 changed color. The subjects were asked to minimize their blinking and head movements. After
149 every 72-second run, there was a short break (typically 30-s to 1 minute). Each subject participated
150 in 15 runs.

151

152



153
154 **Figure 1. Overview of experimental design.** Large-field on-off stimuli were presented in 6-s blocks consisting of either
155 both-, left-, or right-hemifield flicker, alternating with 6-s blocks of blanks (mean luminance). A run consisted of six
156 stimulus and six baseline blocks, after which the subject had a short break. The figure shows the first half of one run.
157 Within a run, the order of both-, left-, and right-field flickering periods was randomized. Fifteen runs were obtained per
158 subject, so that there were 30 repetitions of each stimulus type across the 15 runs. The fixation dot is increased in size for
159 visibility. Actual fixation dot was 0.17 degrees in radius (6 pixels).

160 MEG signal acquisition

161 Data for the main experiment were acquired continuously with a whole head Yokogawa MEG
162 system (Kanazawa Institute of Technology, Japan) containing 157 axial gradiometer sensors to
163 measure brain activity and 3 orthogonally-oriented reference magnetometers located in the dewar
164 but away from the brain area, used to measure environmental noise. The magnetic fields were
165 sampled at 1000Hz and were filtered during acquisition between 1Hz (high pass) and 200Hz (low
166 pass).

167 In a subset of subjects (S6-S8), eye movements were recorded by an EyeLink 1000 (SR Research
168 Ltd., Osgoode, ON, Canada). Right eye position data were continuously recorded at a rate of 1000Hz.
169 Calibration and validation of the eye position was conducted by having the subject saccade to
170 locations on a 5-point grid. Triggers sent from the presentation computer were recorded by the
171 EyeLink acquisition computer. The same triggers were recorded simultaneously by the MEG data
172 acquisition computer, allowing for synchronization between the eye-tracking recording and MEG
173 recording.

174 The 4 data sets acquired with an Elekta Neuromag at CiNet and were pre-processed in MATLAB
175 (MathWorks, MA, USA) using the identical code and procedure. The CiNet data were acquired as
176 102 pairs of planar gradiometer signals (204 sensors). Data were analyzed from each of the 204
177 gradiometers separately and paired into 102 locations for mesh visualization (e.g., the broadband
178 signal-to-noise-ratio for sensor 121 and 122 out of 204 would be averaged to show one signal-to-
179 noise-ratio in the position of sensor 61 out of 102).

180 Data analysis

181 Reproducible computation and code sharing

182 All analyses were conducted in MATLAB. In the interest of reproducible computational methods,
183 both the analysis code and the MEG data for all results reported in this paper will be publicly
184 available via the Open Science Framework at the url <https://osf.io/c59sh/> (doi
185 10.17605/OSF.IO/C59SH). Figures 2-15 (except 3) can be reproduced by running scripts from the
186 GitHub repository of the form *dfdMakeFigure4.m*, or the master script *dfdMakeAllFigures.m*.

187 MEG preprocessing

188 For some analyses, data were environmentally denoised using published algorithms prior to any
189 further analysis. This enabled us to compare data denoised with our new algorithm alone, or with
190 our new algorithm following environmental denoising. For the NYU data, we used either of two
191 algorithms. One was the continuously adjusted least-square method (CALM; ([Adachi et al., 2001](#)),
192 applied to data with a block length of 20 seconds (20,000 time samples). The second algorithm was
193 time-shifted principal component analysis (TSPCA; ([de Cheveigne and Simon, 2007](#)), with a block
194 length of 20 seconds and shifts of up to +/- 100 ms in 1 ms steps. For the CiNet data, the
195 environmental denoising algorithm was temporal signal space separation ('tSSS') (with default
196 parameters, e.g. inside and outside expansion orders of 8 and 3, respectively; 80 inside and 15
197 outside harmonic terms; correlation limit of 0.98).

198 The FieldTrip toolbox ([Oostenveld et al., 2011](#)) was used to read the data files (either
199 environmentally-denoised or raw). For all subsequent analyses, custom code was written in
200 MATLAB. Using either the environmentally-denoised data or raw data, the signals were divided into
201 short epochs. Each stimulus type (left-, right-, or both-hemifield, or blank) was presented in 6-s
202 blocks, and these blocks were divided into 6 non-overlapping 1-s epochs. We discarded the first
203 epoch of each 6-s block to avoid the transient response associated with the change in stimulus.
204 After epoching the data, we used a simple algorithm to detect outliers. We first defined a 'data
205 block' as the 1-s time series from one epoch for one sensor. So a typical experiment consisted of
206 ~170,000 data blocks (157 sensors x 1080 1-s epochs). We computed the standard deviation of the
207 time series within each data block, and labeled a block as 'bad' if its standard deviation was more
208 than 20 times smaller or 20 times larger than the median standard deviation across all data blocks.
209 The time series for bad data blocks were replaced by the time series spatially interpolated across
210 nearby sensor (weighting sensors inversely with the distance). Further, if more than 20% of data
211 blocks were labeled bad for any sensor, then we removed the entire sensor from analysis, and if
212 more than 20% of data blocks were bad for any epoch, then we removed the entire epoch from
213 analysis. Typically, two to seven sensors and 2%-4% of the epochs were removed per session for
214 the NYU data. For the CiNet datasets, almost no sensors or epochs were removed (one sensor and
215 one epoch across all data sets). These preprocessing steps were implemented with
216 [dfdPreprocessData.m](#).

217 Computation of stimulus-locked and broadband responses

218 Data were summarized as two values per sensor and per epoch: a stimulus-locked and a broadband
219 power value. These calculations were done by first computing the Fourier transform of the time
220 series within each epoch (Figure 2A,B).

221 The stimulus-locked signal was then defined as the amplitude at the stimulus-locked frequency
222 (12Hz). The broadband response was computed as the geometric mean of the power across
223 frequencies within the range of 60-150Hz, excluding multiples of the stimulus-locked frequency
224 (see also Figure 2 AB). The geometric mean is the exponential of the average of the log of the signal.
225 We averaged in the log domain because log power is better approximated by a normal distribution
226 than is power, which is highly skewed. These two calculations converted the MEG measurements
227 into a broadband and a stimulus-locked summary metric, each sampled once per second (Figure
228 2C). The two summary metrics were computed by the functions [getstimlocked.m](#) and
229 [getbroadband.m](#).

230 We then bootstrapped across epochs to compute confidence intervals on the signal estimates (per
231 sensor and per condition). For each of 1000 bootstraps, we sampled n epochs with replacement,
232 where n is the total number of epochs in the experiment. We then computed the average response
233 across epochs for each stimulus condition, minus the average across blank epochs. This provided

234 one summary measure for each of the three stimulus conditions and each of the two dependent
 235 measures (broadband and stimulus-locked) for each of the 1000 bootstraps. Finally, we took the
 236 median across bootstraps as the estimate of signal and half of the 68% confidence interval across
 237 bootstraps as the estimate of the noise (Figure 2D,E). For some analyses, the ratio of these values
 238 was defined as the signal-to-noise ratio (SNR).

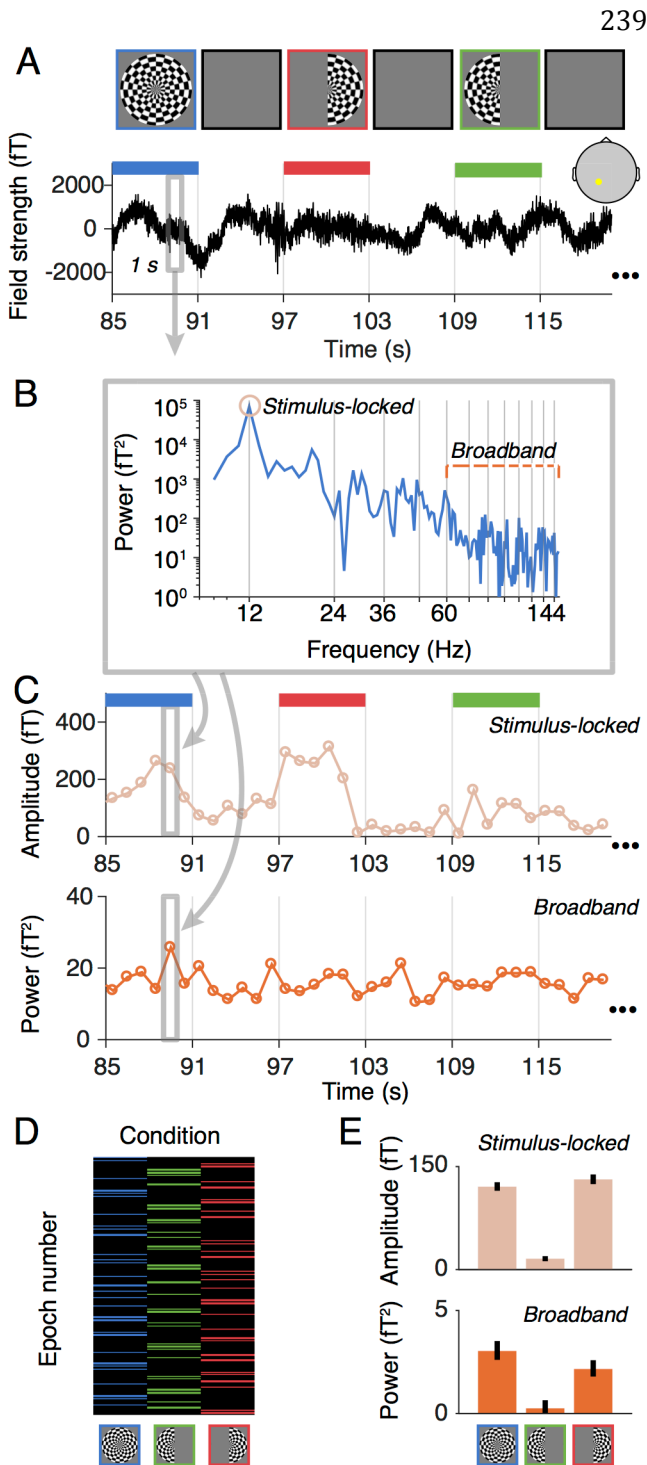


Figure 2. Data analysis without denoising. A. The time series for each sensor were epoched into non-overlapping one-second periods. BC. The time series in each epoch was fast Fourier transformed and then summarized as two values, a stimulus-locked value (amplitude of the fast Fourier component at the stimulus frequency), and a broadband value (mean of the log power of all frequencies from 60-150Hz, excluding those within +/- 1Hz of stimulus harmonics). D. The summary of conditions is shown as a matrix, where each column corresponds to one of the three stimulus conditions, and the number of rows is equal to the total number of epochs across the session. Rows with no color are blank epochs. E. Summary metrics were computed separately for the stimulus-locked values and broadband measures, yielding three measures per sensor per data type. The summary metric was the mean across condition minus the mean across blanks, bootstrapped 1000 times. The bar plot show the median and the 68% confidence interval based on 1000 bootstraps.

MEG Denoise Algorithm

Extracranial measurements like MEG have multiple global noise sources and a relatively low signal-to-noise ratio compared to intracranial measures, especially for high frequency signals. In order to increase the signal-to-noise ratio, we developed a denoising technique that helps reveal the broadband signal of interest. A denoising algorithm developed for fMRI ('GLMdenoise'; (Kay et al., 2013)) was adapted for MEG to project out noise from the data for each epoch in each sensor. The logic behind the algorithm is that many sources of noise are global, and therefore spread across sensors. The algorithm identifies sensors that have no stimulus-related response (the 'noise pool'), and uses these sensors to define noise components. The noise components are then projected out from all sensor time series in each epoch.

283 *Noise pool selection*

284 The noise pool was defined as the 75 (NYU) or 100 (CiNet) sensors with the lowest stimulus-locked
285 SNR across conditions. The SNR was computed by (a) dividing the median response across
286 bootstraps by the variability across bootstraps (half of the 68% confidence interval) for each
287 condition, and (b) taking the maximum of the three values (corresponding to the three stimulus
288 conditions) for each sensor.

289 We used the stimulus-locked signal to identify the noise pool because this signal had a very high
290 SNR, and could easily be measured prior to running our denoise algorithm, and because we
291 assumed (and confirmed by inspection) that sensors with broadband responses also had stimulus-
292 locked responses.

293 For most subjects, most of the sensors in the noise pool were located over the front of the head (see
294 for example Figure 3A).

295 *Filtering of time series*

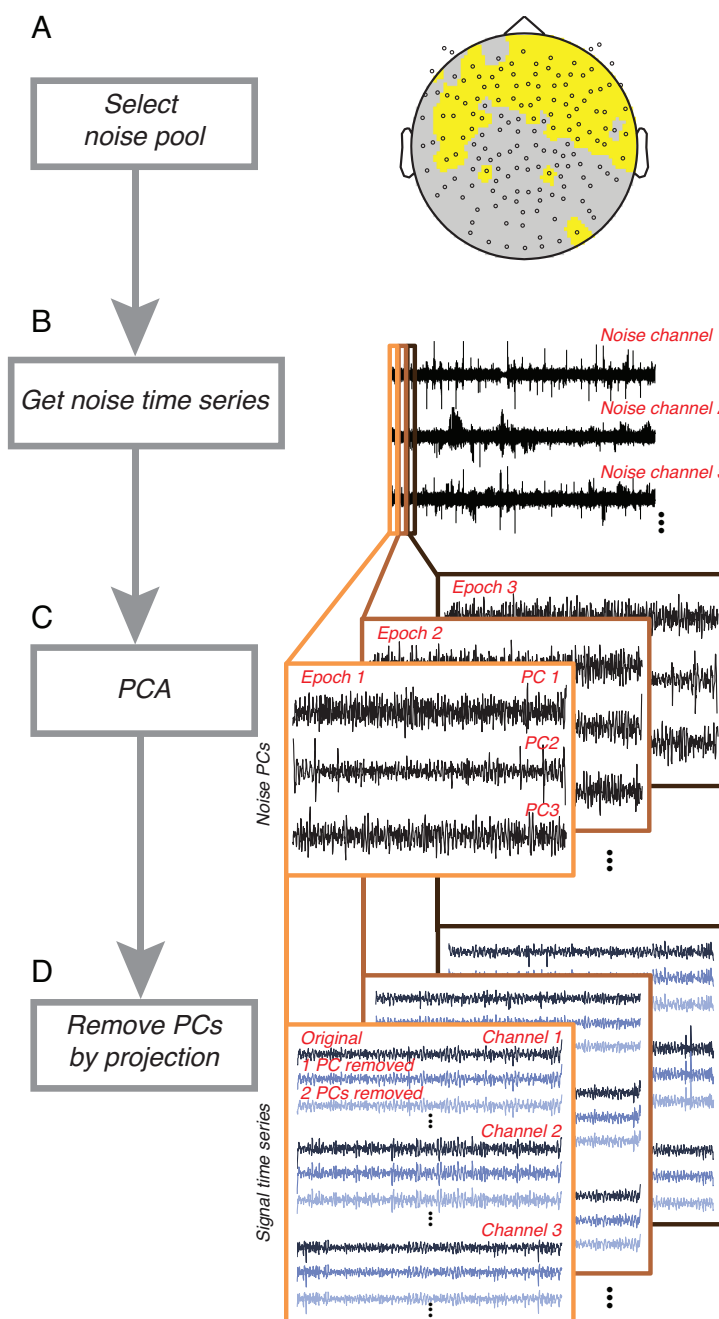
296 As described above, the broadband summary metric was derived from power at a limited range of
297 temporal frequencies (60-150Hz, excluding multiples of the stimulus frequency). After defining the
298 noise pool, the time series of all sensors in all epochs were filtered to remove signal at all
299 frequencies not used to compute the broadband signal. Hence the remaining time series contained
300 power only at frequencies defining the signal of interest. This step was important because the noise
301 pool, though selected for a low stimulus-locked SNR, could nonetheless have contained a small,
302 residual stimulus-locked signal. This residual signal would have been correlated with the
303 experimental design (larger when stimuli were present than absent) and hence projecting it out of
304 the data could have caused a systematic bias (see the script [denoisingProjectingInVariance.m](#)).

305 *PCA*

306 Following filtering, the next step in the algorithm was principal component analysis (PCA). This
307 identified the common components of the time series across the sensors in the noise pool. PCA was
308 computed separately for each 1-s epoch (Figure 3C). This means that denoising occurred at the
309 same temporal scale (1 second) as the computation of the summary metrics. This differs from some
310 denoising algorithms, in which noise regressors are identified over a much longer time period, e.g.,
311 several minutes ([Vigario, 1997](#)). Denoising at a short-time scale can be advantageous if the spatial
312 pattern of the noise responses is not consistent across the entire experiment. As a control
313 comparison, we also ran our algorithm by identifying PC time series on the entire duration of the
314 experiment (~20 minutes) rather than epoch by epoch. (See Results, 'Control analyses for MEG
315 Denoise algorithm'.)

316 *Projecting out PCA components*

317 The first one to ten principal components (PCs) in each epoch were projected out of the time series
318 for all sensors, using linear regression. This resulted in ten new data sets: One with PC 1 projected
319 out, one with PC 1 and 2 projected out, etc. up to 10 PCs projected out (Figure 3D). After projecting
320 out the noise components, we summarized the data into a stimulus-locked and broadband
321 component as described in Figure 2.



322

323

324

325

326

327

328

Figure 3. Denoising procedure. Following an estimate of response reliability computed from non-denoised data (Figure 2), the algorithm first selects a noise pool. **A.** The noise pool is comprised of sensors whose SNR from the evoked (stimulus-locked) component falls below a threshold. **B.** The time series from each sensor in the noise pool is then filtered to remove components that do not contribute to the broadband computation. **C.** Principal component analysis is then computed within each epoch. **D.** For each epoch, the first n PCs are projected out from the time series of all sensors, yielding n new data sets. For each new data set, broadband responses were recomputed, as in Figure 2.

329 **Statistical comparisons**

330 To assess the effect of the MEG Denoise algorithm on the broadband SNR, we compared the
331 broadband SNR after applying MEG Denoise to the broadband SNR either without denoising or after
332 applying other denoising algorithms. To make these comparisons, we first identified 10 sensors of
333 interest from each subject. These sensors of interest were the 10 with the highest SNR in any of the
334 three stimulus conditions, either before or after denoising, excluding sensors from the noise pool.
335 For each of the three stimulus conditions, we then took the average SNR from these 10 sensors
336 without denoising or after applying MEG Denoise or another denoising algorithm. Finally, we
337 conducted two-tailed t-tests, paired by subject (n=8), between the broadband SNR after MEG
338 Denoise to the broadband SNR without denoising (or with another algorithm). The t-tests were
339 conducted separately for each of the three stimulus conditions (both-hemifield, left-hemifield, and
340 right-hemifield).

341 **Control analyses**

342 To investigate the validity of our algorithm, we ran multiple control analyses. In particular, it is
343 important to rule out the possibility that the denoising algorithm produces significant results even
344 when the data contains no sensible signal. To test this, we compared the difference in SNR of
345 denoised data with the following controls: (1) phase-scrambling the PC time series, and (2) using all
346 sensors to define the noise with PCA rather than only a subset of sensors that have little to no
347 stimulus-locked signal. We also assessed the effect of identifying and projecting out PC time series
348 equal in length to the entire experiment (~20 minutes), rather than PC time series matched in
349 length to our analysis epochs (1-s). This comparison tested the assumption that denoising in
350 shorter epochs was advantageous, possibly due to the pattern of noise sources differing over the
351 course of the experiment.

352 **Eye tracking analysis**

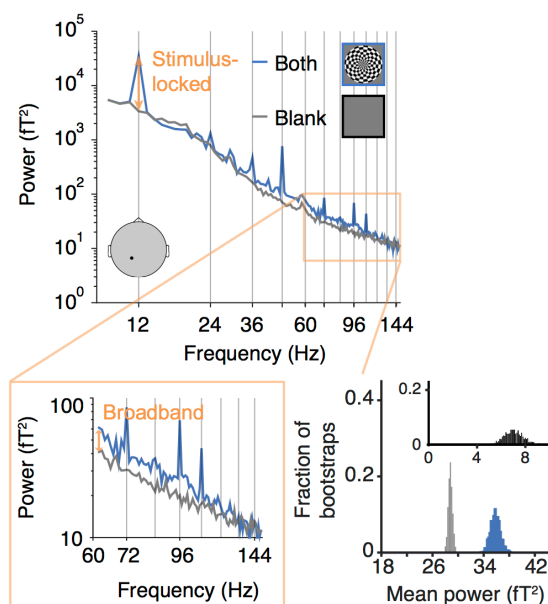
353 Since an increase in microsaccade rate can induce broadband spectral components in extracranial
354 measurements such as EEG or MEG ([Yuval-Greenberg et al., 2008](#); [Keren et al., 2010](#)), we checked in
355 three NYU subjects (S6-S8) whether there was a difference in rate between the 'off' baseline
356 periods and 'on' stimulus periods, and within the three stimulus (both-, right-, left-hemifield)
357 conditions. Microsaccades were identified as changes in position with above a relative velocity
358 threshold ($6^\circ/\text{s}$) and a minimum duration of 6 ms, as reported in Engbert & Mergenthaler ([2006](#)) to
359 analyze rate and direction of microsaccades as well as separating MEG data into epochs that did and
360 did not contain microsaccades.

361 Results

362 A large field ‘on-off’ stimulation experiment was used to characterize the stimulus-locked (steady
363 state evoked field, ‘SSVEF’) and broadband responses in visual cortex measured with MEG. The two
364 measures are reported below, both prior to and after applying our new denoising algorithm.

365 Stimulus-locked and broadband signals measured with MEG

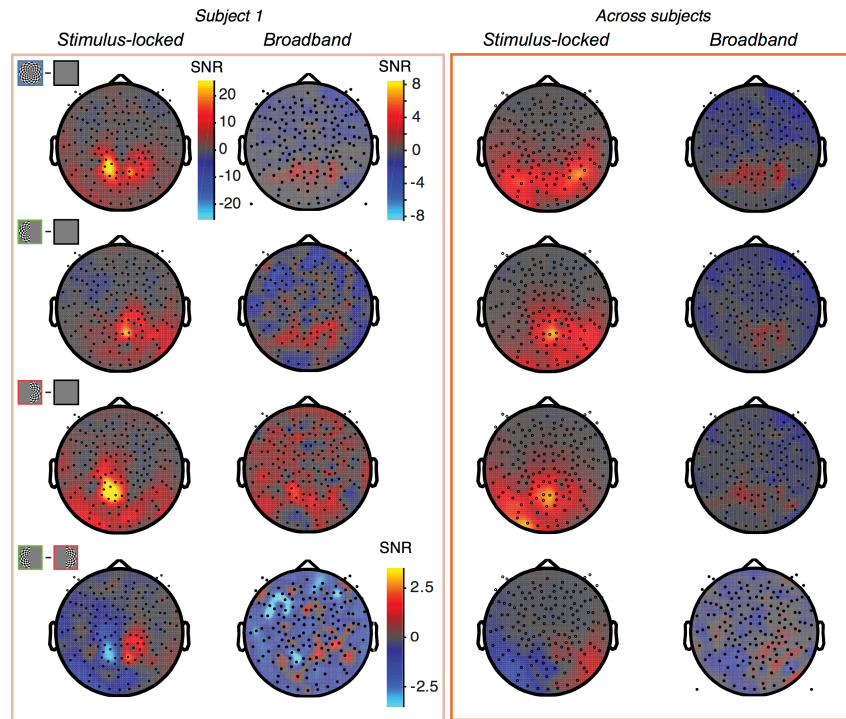
366 In each stimulus condition (left-, right-, and both-hemifield), the stimulus contrast reversed 12
367 times per second, so the stimulus-locked signal was measured at 12Hz and harmonics. Because the
368 largest component was at 12Hz, we defined the stimulus-locked signal for a particular stimulus
369 condition as the amplitude at 12Hz, averaged over all 1-second epochs with that stimulus (typically
370 ~180 epochs) computed for each of the 157 sensors in each subject (Figure 4; see Methods for
371 details). The broadband signal was computed by averaging the log power across frequencies
372 between 60 and 150Hz, excluding multiples of the stimulus frequency (12Hz), and then
373 exponentiating the mean (Figure 4 inset; see Methods for details).



374 **Figure 4. Example response to flickering large-field stimulus.** The main panel plots the spectral power, averaged
375 across 180 1-s epochs, during which the subject viewed either the both-hemifield stimulus (blue line) or a blank screen at
376 mean luminance (gray line). The black dot on the schematic head indicates the location of the sensor. The peak at 12Hz
377 corresponds to the frequency of dartboard contrast reversals, and is a measure of the stimulus-locked component (orange
378 arrow). The lower inset zooms in on higher frequencies to emphasize the broadband component, most evident in this
379 example data set as a spectral power elevation spanning 60 to 150Hz. The increase in the broadband response of the
380 stimulus condition relative to the blank condition is shown by the orange arrow. The histograms on the right show the
381 broadband level separately for the stimulus condition (blue) and the blank condition (gray), and the difference between
382 them (black), computed 1000 times by bootstrapping over epochs in the experiment. Data from subject S1. Made with
383 function *dfdMakeFigure4.m*.
384

385 Both the stimulus-locked and broadband signals were largest in medial, posterior sensors, as
386 expected from activations in visual cortex (Seki et al., 1996). For the stimulus-locked signal, the
387 both-hemifield condition tended to produce broadband signals in bilateral posterior sensors,
388 whereas the single-hemifield conditions produced responses that were lateralized, with higher SNR
389 contralateral to the stimulus. This pattern could be seen in an example subject and in the average
390 across subjects (Figure 5). The lateralization of the stimulus-locked signal was less clear in the
391 average across subjects due to imperfect alignment of the sensors showing the largest differential

392 response to the left- and right- hemifield stimuli. In each of the 8 individual subjects and in each of
393 the 3 conditions, the stimulus-locked response was evident, with the signal at least 10x above the
394 noise (data not shown).



395
396 **Figure 5. Topographic map of stimulus-locked and broadband responses.** Data from subject S1 (left) and averaged
397 across subjects S1-S8 by sensor (right). The top 3 rows show data from the 3 stimulus conditions (both-, left-, and right-
398 hemifield) compared to blank, and the lower row shows data as the left-only minus right-only conditions. The dependent
399 variable plotted for the single subject data is the signal-to-noise ratio at each sensor, computed as the mean of the
400 contrast (stimulus minus blank) across bootstraps divided by the standard deviation across bootstraps (bootstrapped
401 over epochs). For the group data, the signal-to-noise ratio is the mean of the subject-specific SNRs at each given sensor.
402 The same scale bar is used for all stimulus-locked plots. For the broadband plots, one scale bar is used for the first three
403 rows, and a different scale bar with a smaller range is used for the fourth row. Made with *dfdMakeFigure5.m*.

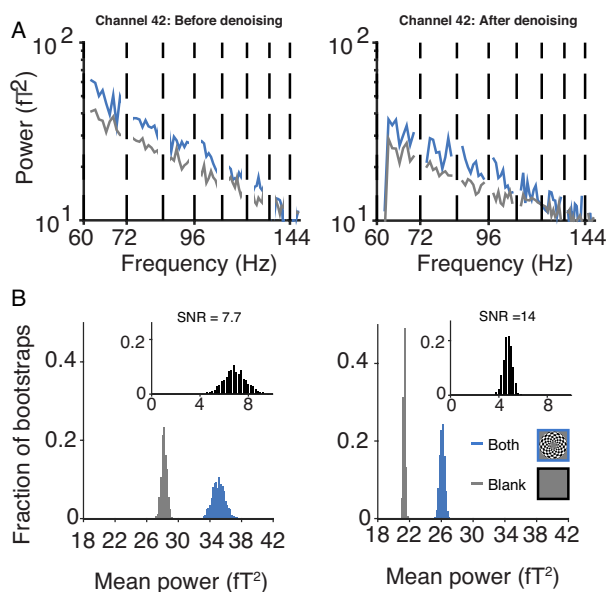
404 The spatial pattern of broadband signals was qualitatively similar to the spatial pattern of the
405 stimulus-locked signal, with bilateral posterior responses in the both-hemifield condition, and
406 lateralized responses in the single-hemifield conditions (Figure 5, individual example and group-
407 averaged data). However, the broadband responses had much lower signal-to-noise than the
408 stimulus-locked responses, and in many of the individual subjects, broadband was not evident in
409 one or more conditions (data not shown). The broadband responses were less reliable for the left-
410 and right-hemifield conditions than for the both-hemifield conditions.

411 The fact that broadband responses were evident in a few subjects in some conditions indicates that
412 it is possible to measure broadband fields with MEG. However, if this signal cannot be measured
413 reliably in many subjects and many conditions, then the practical value of measuring broadband
414 with MEG is limited. This motivated us to ask whether denoising the MEG data could unmask
415 broadband signals, making it more reliable across subjects and stimulus conditions.

416

417 Denoising increases the broadband SNR by reducing variability

418 The MEG data were denoised using a new algorithm as described in detail in the Methods section.
419 In brief, for each subject a subset of sensors that contained little to no stimulus-locked responses
420 were defined as the noise pool. Once the noise-pool was defined, the time series in each sensor and
421 in each epoch was filtered to remove all signals not contributing to the broadband measurement.
422 Global noise regressors were then derived by principal component analysis from the filtered time
423 series in the noise pool in each 1-s epoch. The first 10 PCs were projected out of the data in each
424 sensor, epoch by epoch. The remainder of the analysis was identical to that used in the non-
425 denoised data set (Figure 2).



426

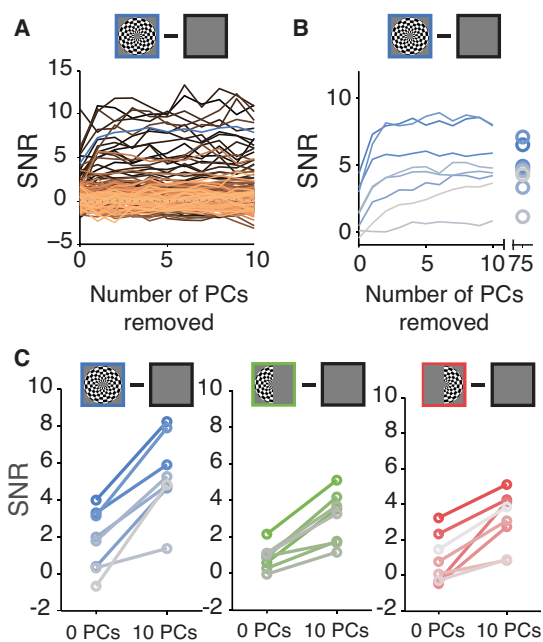
427 **Figure 6. Effect of denoising on broadband response.** (A) The upper panel shows the power spectra from sensor 42,
428 subject 1, averaged across 178 epochs with the both-hemifield stimulus (blue) and blank screen (gray). The left panel is
429 prior to denoising and is identical to the inset in figure 4, except that harmonics of stimulus-locked frequencies have been
430 removed. The right panel is the same as the left, except after denoising. (B) The lower panel shows the distributions of the
431 bootstrapped broadband power for the both-hemifield (blue), blank (gray), and both-hemifield minus blank (black, inset),
432 prior to denoising (left) and after denoising (right). The SNR is defined as the median of the difference distribution
433 divided by half of the 68% confidence interval in the difference distribution (7.7 prior to denoising, 14.0 after). The effects
434 of denoising are to reduce the mean power, and more importantly, reduce the standard deviation across epochs. Made
435 with *dfdMakeFigure6.m*.

436 We first illustrate the effect of denoising with an example from a single sensor in one subject
437 (Figure 6). This sensor showed a broadband response both prior to, and after, denoising. The
438 benefit of denoising was not evident when comparing the mean power spectra before and after
439 denoising (Figure 6A). Denoising did not reduce the variability in power across frequencies, nor did
440 it increase the separation in the spectra for the contrast stimulus and the blank. Instead, the effects
441 of denoising are better appreciated by examining the variability across epochs rather than across
442 frequencies (Figure 6B). The biggest effect is that the broadband power estimates became less
443 variable across epochs, both for the blank condition and the stimulus condition. This is indicated by
444 the narrower distributions in the response amplitudes for the two conditions (Figure 6B, main
445 panels) and for the difference between conditions (Figure 6B, insets). The standard deviation of the
446 difference distributions decreased more than two-fold (from 0.79 to 0.35) as a result of denoising.

447 There are two other secondary patterns evident in these distributions. First, the mean broadband
448 power of both the blank and stimulus condition decreased as a result of denoising (for the both-
449 hemifield condition, 35.8 versus 26.1, prior to versus after denoising; for the blank, 28.7 versus
450 21.4). This was expected because projecting out signal reduces power. Second, the contrast
451 between the two conditions (difference between the means) reduced: 7.0 prior to denoising versus
452 4.8 after denoising. The combination of these two effects was that the *percent difference* was little
453 changed, with broadband power from the contrast-stimulus about 25% more than for the blank
454 before and after denoising. Hence denoising did not increase the estimate of the percent signal
455 change.

456 It is important to consider how these effects interact. Because the reduction in variability across
457 epochs was the biggest effect of denoising (more than 2-fold), there was more than a doubling of
458 SNR, computed as the median divided by the variability of the difference distribution. In sum, the
459 spectral plots show that the variability in power *across frequencies* was little affected by denoising
460 (Figure 6A), whereas the distribution plots show that the variability in total broadband power
461 *across epochs* was reduced considerably (Figure 6B).

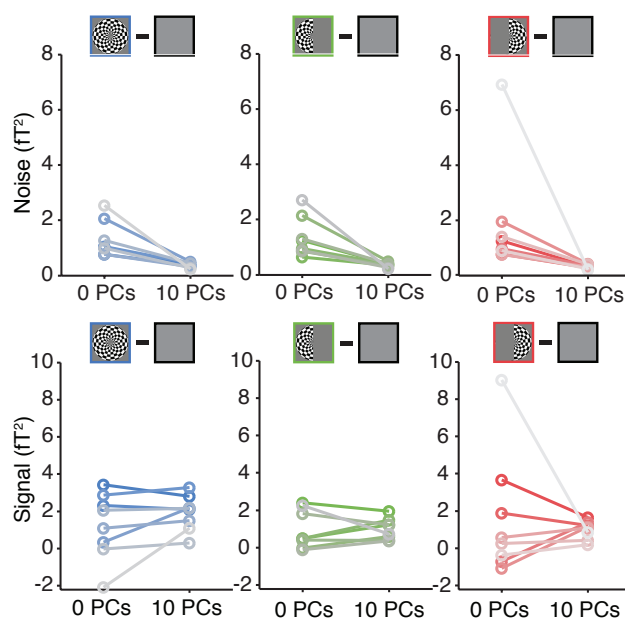
462 We now consider the effect of denoising across sensors, subjects, and stimulus conditions.
463 Projecting out noise PCs substantially increased the signal-to-noise ratio of the broadband
464 measurement in visually responsive sensors. For example, in the both-hemifield condition for
465 subject S1, the median SNR of the 10 most visually responsive sensors increased from 5 to 10 after
466 denoising (Figure 7A, blue solid line), similar to the example sensor shown earlier (Figure 6B). In
467 contrast, the SNR of the 75 sensors in the noise pool was relatively unaffected by denoising (Figure
468 7A, blue dashed line). This was expected because sensors in the noise pool were unlikely to
469 distinguish stimulus from blank. Across the 8 subjects in the both-hemifield condition, taking the
470 mean of the 10 most visually responsive sensors for each subject, the SNR increased about 3-fold
471 (from 1.6 to 5.0), with a numerical increase in every subject (Figure 7B). Because the SNR stabilized
472 in all subjects with 10 or fewer PCs projected out, in subsequent analyses, for simplicity we report
473 the effects of denoising with exactly 10 PCs. A comparison of the SNR before denoising (0 PCs
474 projected out) and after (10 PCs projected out) summarized across all subjects and the three
475 stimulus conditions shows increases in SNR for every subject in all conditions (Figure 7C)
476 ($p=0.0001$, $p=0.0007$, $p=0.0022$ for two-tailed t-tests, 0 v 10 PCs, for both-, left-, and right-hemifield
477 conditions, respectively).



478

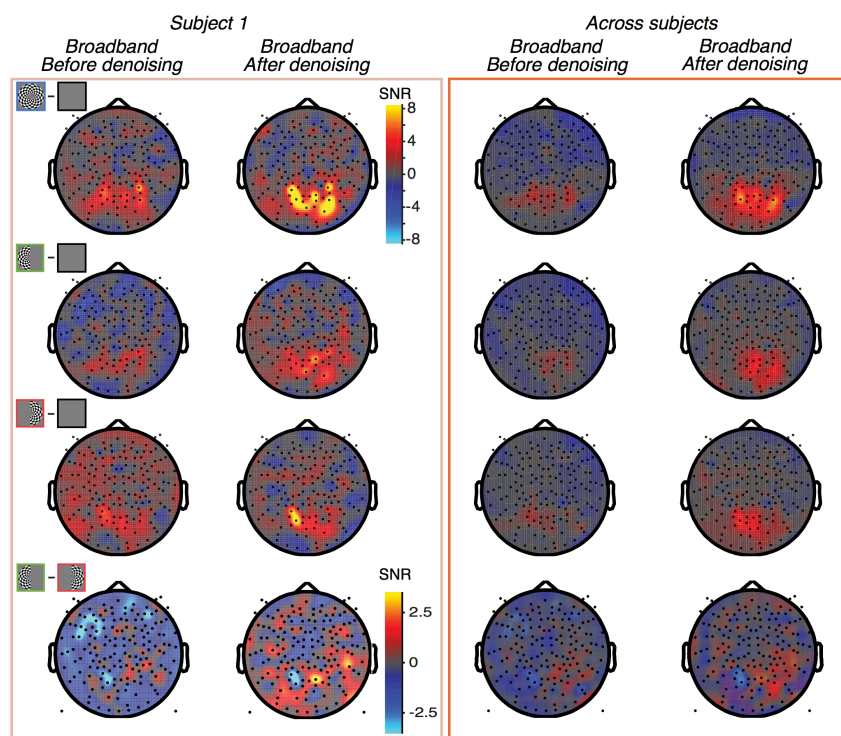
479 **Figure 7. Effect of denoising on broadband SNR.** (A) SNR as a function of the number of PCs projected out in subject S1
480 for the both-hemifield stimulus. Each line is one sensor. The heavy blue line is the mean of the 10 sensors with the highest
481 SNR, as measured either before or after denoising. (B) SNR as a function of PCs projected out in each of 8 subjects for the
482 both-hemifield stimulus. Each line is the mean across the 10 sensors with the highest SNR in one subject. The rightmost
483 points indicate the effect of projecting out all 75 PCs. (C) SNR before denoising (0 PCs projected out) and after denoising
484 (10 PCs projected out) for each stimulus condition. Each line is the mean of the 10 sensors with the highest SNR for one
485 subject in one stimulus condition. Color saturation corresponds to the subject number (highest to lowest saturation,
486 subjects 1-8, respectively). Made with *dfdMakeFigure7.m*.

487 In principle, the SNR increases could have arisen from increased signal, decreased noise, or both. To
488 distinguish among these possibilities, we compared the signal level alone and the noise level alone
489 before and after denoising. As in prior results, the signal was defined as the difference in broadband
490 power between the contrast pattern and the blank (median across bootstraps), and the noise was
491 defined as the variability of this difference metric (half of the 68% confidence interval across
492 bootstraps). For all three stimulus conditions in most subjects, the signal was largely unaffected by
493 denoising, staying at a similar level or decreasing slightly, while the noise level went down
494 substantially (Figure 8). These analyses indicate that the increase in SNR from denoising (Figure 7)
495 was caused by a reduction in epoch-to-epoch variability of the broadband signal level, and not by an
496 increase in the signal level, consistent with the results of the single example sensor (Figure 6).
497 Expressed as a percentage increase over baseline, the broadband response to the both-hemifield
498 stimulus after denoising was $\sim 10.9 \pm 1.7\%$ averaged across the top 10 sensors in each subject (mean
499 \pm sem across subject), and $12.6\% \pm 1.6\%$ for the top 5 sensors. This contrasts with the much larger
500 stimulus-locked response, which was a nearly 8-fold increase over baseline even prior to denoising
501 ($678\% \pm 226\%$ increase over baseline for the top 5 sensors).

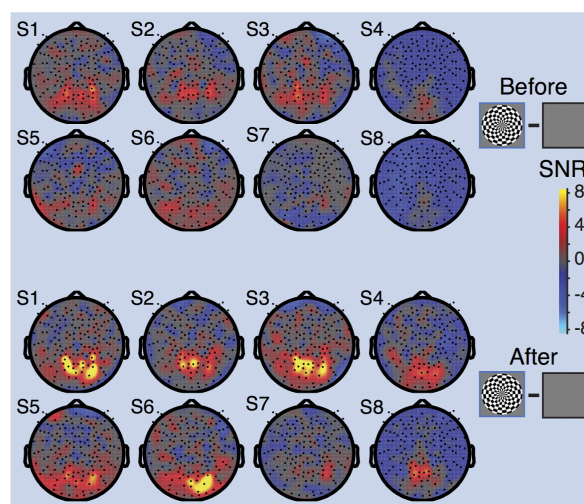


502
503 **Figure 8. Effect of denoising on the broadband signal and noise.** Noise (upper) and signal (lower) before and after
504 denoising in each of three stimulus conditions. Plotting conventions as in Figure 7c. Made with *dfdMakeFigure8.m*.

505 The effect of denoising the broadband signal was not uniform across the sensor array. In general,
506 sensors where we expected visual activity (over the posterior, central part of the head) showed
507 increased SNR following denoising. In the example subject S1 as well as the average across subjects,
508 the denoised broadband response was observed in bilateral sensors for the both-hemifield
509 condition, and with a contralateral bias (relative to the midline) in the two lateralized conditions
510 (Figure 9). For the both-hemifield stimulus, broadband responses were evident in sensors over the
511 posterior, middle of the head in most individual subjects (Figure 10).



512
 513 **Figure 9 Topographic map of broadband SNR before and after denoising.** Data from subject S1 (left) and averaged
 514 across subjects S1-S8 by sensor (right). The top 3 rows show data from the 3 stimulus conditions (both-, left-, and right-
 515 hemifield) and the fourth row shows the difference between the left-only and right-only conditions. The fourth row uses a
 516 different scale bar from the other 3 rows. The columns show data before and after denoising. Made with
 517 *dfdMakeFigure9.m*.

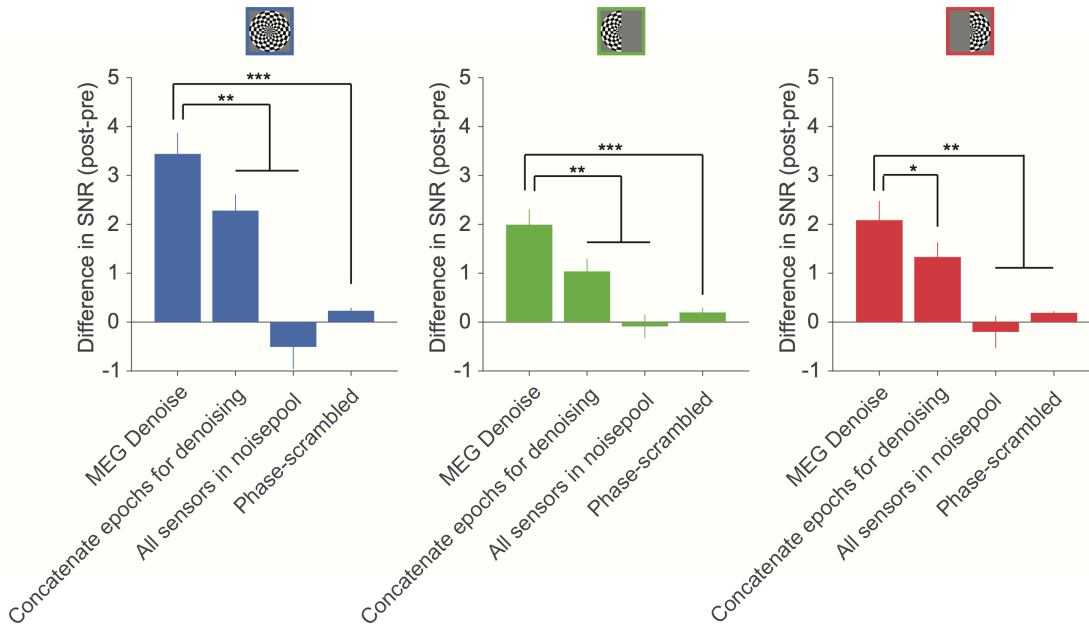


518
 519 **Figure 10 Topographic maps of broadband SNR in individual subjects after denoising.** Head plots show the SNR for
 520 the both-hemifield stimulus, before denoising (above) and after denoising (below). Made with *dfdMakeFigure10.m*.

521 Control analyses for MEG Denoise algorithm

522 To validate the assumptions in our denoising algorithm, we ran three control analyses. In one
 523 control analysis, we concatenated all epochs to derive noise regressors from the whole
 524 experimental time series (Figure 11, 2nd bar, compared to using the default of 1-s epochs to derive
 525 noise regressors – 1st bar). The elevation in broadband SNR was significantly less when we

526 concatenated all epochs ($p = 0.0016$, $p = 0.0023$ and $p = 0.0447$, for the three stimulus conditions
527 respectively). In the second control analysis, the noise pool included all sensors rather than only
528 those sensors that were not visually responsive. Here, the noise regressors included some signal as
529 well as noise, and hence should be of less benefit. This expectation was confirmed, in that there was
530 no increase in SNR when the algorithm was run with the omission of the noise-pool-selection step
531 (Figure 11, 3rd bar, $p = 0.0014$, $p = 0.0015$ and $p = 0.0020$ for the three stimulus conditions
532 respectively). In a 3rd control analysis, we phase-scrambled each of the epoch-by-epoch noise time
533 series. The phase-scrambled regressors were temporally uncorrelated with the actual time series in
534 the noise. As a result, we found no change in SNR levels (Figure 11, fourth bar, $p = 0.0001$, $p =$
535 0.0003 and $p = 0.0017$).

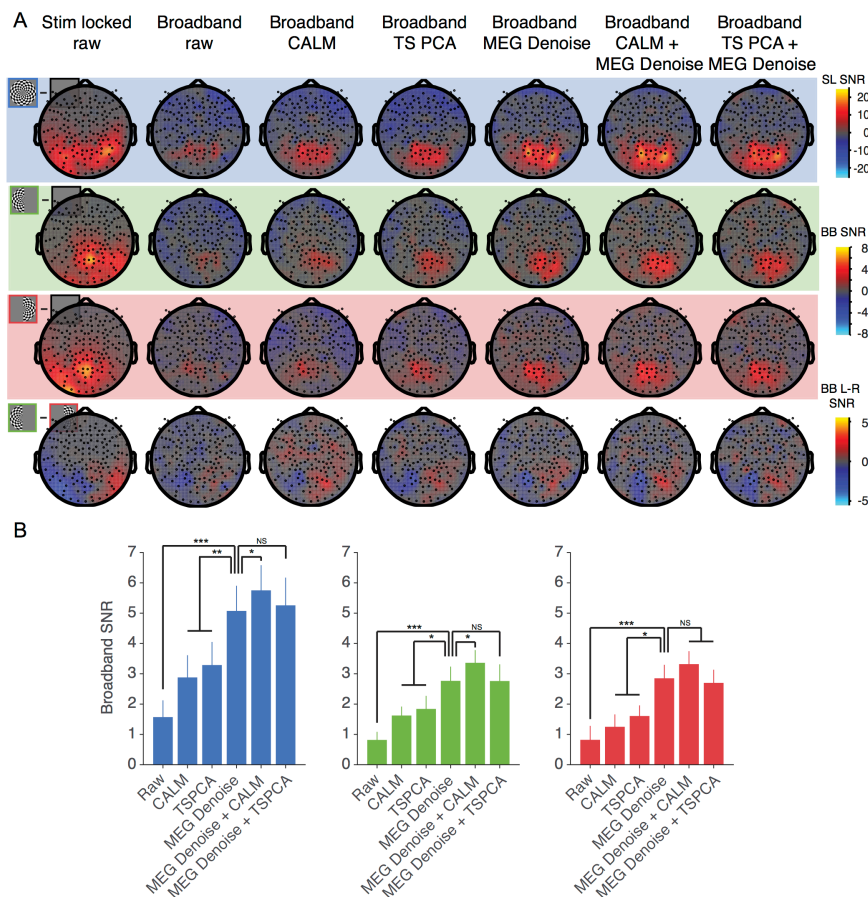


536
537 **Figure 11. Comparison of MEG Denoise to control analyses.** When the denoising algorithm derives noise regressors
538 from the whole experimental time series ('Concatenate epochs for denoising'), the amount of SNR gain is significantly less
539 than the standard MEG Denoise (regressors derived separately from each 1-s epoch). When the noise regressors are
540 derived from all sensors ('All sensors in noisepool'), or when the time series of the regressors are phase-scrambled, there
541 is little or no change in SNR for all three stimulus conditions. Statistical significance is computed by a 2-tailed t-test,
542 paired by subject, between denoising analyses. Statistical significance is indicated by * = $p < 0.05$, ** = $p < 0.01$, *** = $p <$
543 0.001 between the MEG Denoise algorithm and each of the other controls. Made with *dfdMakeFigure11.m*.

544 Other denoising algorithms

545 To assess how other existing denoising algorithms affect our measurement of broadband power,
546 and how they interact with our new denoising algorithm, we ran two different denoising
547 algorithms, either alone or in combination with MEG Denoise. The two algorithms we tested were
548 CALM, or continuously adjusted least-square method (Adachi et al., 2001) and TSPCA, or time-shift
549 principal component analysis (de Cheveigne and Simon, 2007). Both of these make use of reference
550 MEG sensors which face away from the head and measure environmental rather than physiological
551 fields. By design, these algorithms project out time series from the subspace spanned by the
552 reference sensors, thereby reducing environmental noise, but not physiological noise. Applying
553 either one of these two algorithms alone to the 8 data sets reported above increased the broadband
554 signal-to-noise ratio, evident in the group-averaged sensor plots (Figure 12A, columns 3-4 versus
555 column 2), and the increased SNR in the 10 most responsive sensors (Figure 12B, 2nd and 3rd bar
556 versus 1st bar in each plot).

557 In planned comparisons, we evaluated the SNR increase of each algorithm or combination of
 558 algorithms to the increase from MEG Denoise alone. The increase from each of the two
 559 environmental algorithms alone was significantly less than that from our new MEG Denoise
 560 algorithm (Figure 12A, column 5 versus columns 3-4; Figure 12B, 4th bar versus 2nd and 3rd).
 561 Applying two algorithms in sequence, first either CALM or TSPCA, followed by MEG Denoise, also
 562 resulted in a large increase in broadband SNR (Figure 12A, columns 6 and 7). For all three stimulus
 563 conditions, the combination of MEG Denoise and CALM resulted in the largest gain in SNR,
 564 significantly larger than MEG Denoise alone for two out of the three conditions (Figure 12B, 5th
 565 versus 4th bars). This indicates that the MEG Denoise algorithm and an environmental algorithm
 566 captured some independent noise.

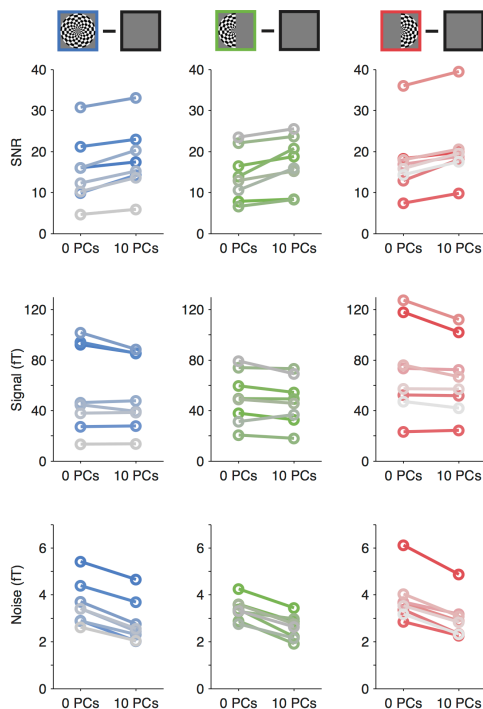


567
 568 **Figure 12. Comparison of different denoising algorithms on NYU datasets (averaged across subjects S1-S8).** (A)
 569 The columns represent SNR values for the stimulus-locked signal (column 1), broadband signal without denoising
 570 (column 2), and broadband signal with one or more denoising algorithms. One scale bar is used for all stimulus-locked
 571 plots (column 1). A second scale bar is used for all broadband plots (columns 2-7) except for the Left minus Right plots
 572 (row 4, columns 2-7). Other details as in Figure 5. (B) Broadband SNR using different algorithms for both-hemifield (left),
 573 left-hemifield (center) and right-hemifield (right) stimuli. Each bar is the change in SNR from baseline (column 2 in panel
 574 A), averaged across the top 10 sensors per subject (mean +/- SEM across subjects). Top sensors were defined as the 10
 575 sensors from each subject with the highest SNR across any of the 3 stimulus conditions and any of the denoising
 576 algorithms (columns 2-7). Statistical significance computed and indicated as in Figure 11. Made with *dfdMakeFigure12.m*.

577 Effect of denoising on stimulus-locked SNR

578 In a separate analysis, we ran the MEG Denoise algorithm to evaluate its effect on the stimulus-
 579 locked signal. The methods were identical to those used to denoise the broadband signal except for
 580 the omission of one step, the step in which we filtered the time series to remove temporal

581 components that do not contribute to the broadband signal. Denoising modestly increased the
582 stimulus-locked SNR for all stimulus conditions for most subjects (Figure 13, top). The SNR
583 increased numerically in all subjects (n=8) and in all stimulus conditions, although the percentage
584 increases were smaller than those for denoising the broadband signal, ~20% increase compared to
585 two-fold. As in the case of denoising the broadband signals, the main contribution to the increase in
586 SNR for the stimulus-locked signal was a decrease in variability across epochs (Figure 13, bottom),
587 rather than an increase in the signal level (Figure 13, middle).



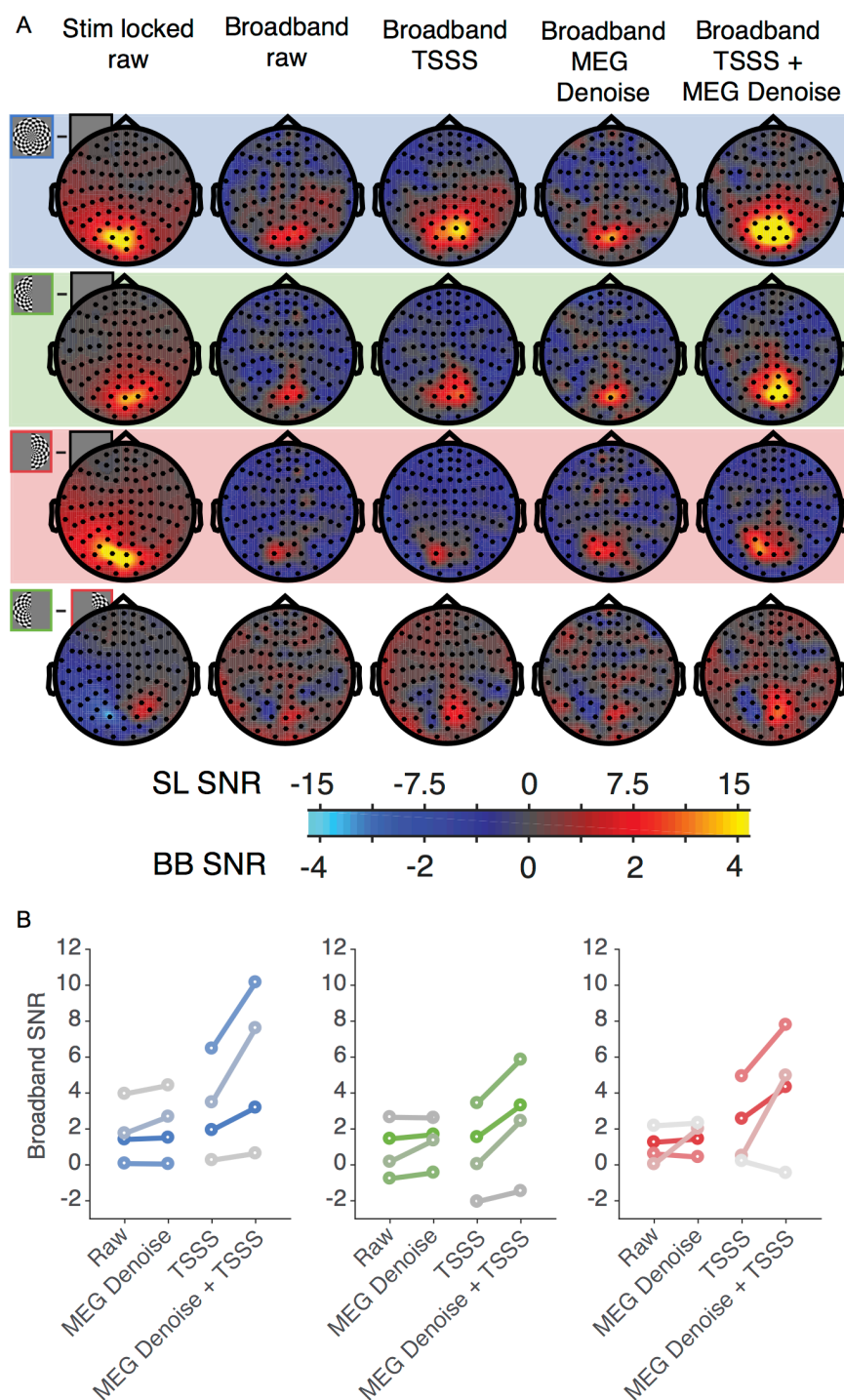
588
589 **Figure 13. Denoising the stimulus-locked signal.** The MEG Denoise algorithm results in a modest increase in SNR for
590 most subjects in all three stimulus conditions (top row). This benefit is largely due to the fact that the noise level goes
591 down from denoising (middle bottom) rather than the signal increasing (middle row). Plotting conventions as in Figure 7c
592 and Figure 8. Made with *dfdMakeFigure13.m*.

593 **Broadband fields measured with Elekta 360 Neuromag**

594 To test whether the findings reported above generalize to other instruments and experimental
595 environments, we conducted the same experiment using a different type of MEG system, an Elekta
596 360 Neuromag at CiNet. The CiNet system contains paired planar gradiometers, in contrast to the
597 axial gradiometers used in the Yokogawa MEG at NYU, and the scanner is situated in a different
598 physical environment, with potentially very different sources of environmental noise. The pre-
599 processing pipeline at this imaging center often includes a denoising step based on temporally
600 extended signal source separation (tSSS) (Taulu and Simola, 2006; Taulu and Hari, 2009). This
601 additional experiment gave us the opportunity to ask several questions: (1) Are broadband fields
602 observed with a different MEG sensor type and different physical environment? (2) Does the tSSS
603 algorithm increase the broadband SNR? (3) Does our new MEG Denoise algorithm increase the SNR
604 of data that have already been denoised with the tSSS algorithm?

605 The identical experiments were conducted with 4 new subjects. As expected, all three stimulus
606 types led to a large stimulus-locked response in the posterior sensors, with a peak SNR of more
607 than 10 in the group averaged data (Figure 14A, column 1). A modest, spatially specific broadband
608 signal was measured from the undenoised data for each stimulus type (Figure 14A column 2), with

609 a peak SNR of 1-2 in the group-average data for all three conditions. Unlike the NYU data, in the
610 CiNet data the MEG Denoise algorithm on the raw data did not generally result in an increase in the
611 broadband SNR (group data, Figure 14A, columns 2 and 3; individual subjects, Figure 14B, left side
612 of each subplot). However, when the raw data were pre-processed with the tSSS algorithm (Figure
613 14A, column 4), application of MEG Denoise increased the SNR in all 3 stimulus conditions for 3 out
614 of 4 subjects, and in 2 out of 3 stimulus conditions for the 4th subject. Together, the MEG Denoise
615 algorithm increased the SNR by 2-3 fold, similar to the NYU data (both-hemifield: 2.8 to 5.6; left-
616 hemifield: 0.8 to 2.4; right-hemifield: 2.01 to 4.4; means across subjects 1-4, top 10 sensors each, for
617 the tSSS data and the MEG Denoised tSSS data). Just as with the NYU MEG data set, the combination
618 of an algorithm tailored to find environmental noise (tSSS) and our algorithm produced the most
619 robust results, indicating that MEG Denoise and the environmental denoising algorithm removed at
620 least some independent sources of noise.



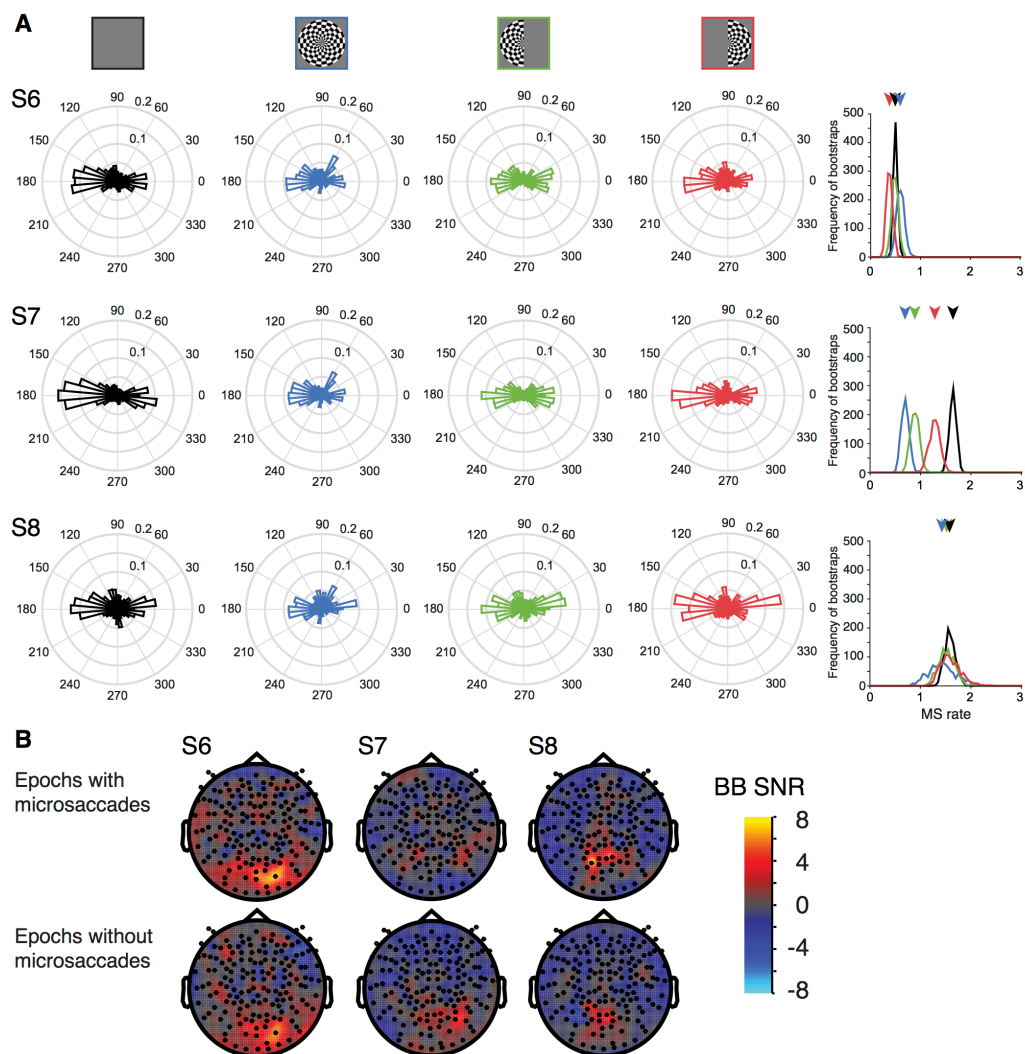
621

622 **Figure 14. MEG data from CiNet Neuromag.** (A) All plots show data averaged across new 4 subjects (S9-S13) in sensor
 623 space (sensor-wise mean of the subject SNR). The columns represent SNR values for the stimulus-locked signal (column
 624 1), broadband signal without denoising (column 2), and broadband signal with one or more denoising algorithms. The
 625 same scale bar is used for all broadband data (columns 3 - 5). Other details as in Figure 5. (B) Broadband SNR using
 626 different algorithms for both-hemifield (left), left-hemifield (center) and right-hemifield (right) stimuli. Each line is
 627 average broadband SNR across the top 10 sensors for one individual. Top sensors were defined as the 10 sensors from
 628 each subject with the highest SNR across any of the 3 stimulus conditions and any of the denoising algorithms (columns 2-
 629 6). Made with *dfdMakeFigure14.m*.

630 Saccadic eye movements during MEG experiments

631 Saccadic eye movements are known to have a large influence on MEG and EEG measurements. This
632 influence can be especially pernicious when measuring high frequency broadband signals, because
633 the spike field (MEG) or spike potential (EEG) arising from extraocular muscle contraction can be
634 spectrally broadband and can co-vary with task design; hence, it can easily be confused with
635 broadband signals arising from brain activity ([Yuval-Greenberg et al., 2008](#); [Yuval-Greenberg and
636 Deouell, 2009](#)). For visual experiments, the spike potential in EEG is especially problematic because
637 it tends to affect sensors which are also visually sensitive (posterior middle). In contrast, the MEG
638 spike field is lateral, potentially influencing temporal and frontal sensors, with little to no effect on
639 posterior sensors ([Carl et al., 2012](#)). Hence spike field artifacts are unlikely to contaminate our
640 visually elicited broadband signals, which are most clearly evident in the central posterior sensors.

641 Nonetheless, for a subset of subjects (S6-S8), we measured eye movements during the MEG
642 experiments and quantified the frequency of microsaccades, and the distribution of microsaccade
643 direction, for each stimulus condition. Each of these 3 subjects showed broadband responses in
644 their denoised data (Figure 10). All three subjects showed a higher rate of horizontal than vertical
645 microsaccades in every stimulus condition (Figure 15), consistent with prior observations
646 ([Engbert, 2006](#)), but there was no systematic pattern in saccade frequency as a function of stimulus
647 condition; for example, the stimulus condition with the most and with the fewest microsaccades
648 differed across the 3 subjects. Moreover, the subject with the highest broadband SNR among these
649 3 (S6) had the lowest rate of microsaccades (~ 0.5 microsaccades / second). To test more directly
650 whether microsaccades contributed to the measured broadband fields, we re-analyzed the data
651 from these 3 subjects in two ways, either limited to only those epochs with microsaccades or only
652 those epochs without microsaccades (Figure 15b). The broadband responses were evident in each
653 subject in the epochs without microsaccades, indicating that this response is not entirely an artifact
654 of microsaccades.



655

656 **Figure 15. Microsaccades during experimental conditions.** (A) The circular histograms show the frequency of
657 microsaccades per 1-s epoch, binned by direction, for each of the 4 stimulus conditions (columns 1-4). The rows show
658 data for 3 subjects. The last column shows the rate of microsaccades (per 1-s epoch) irrespective of direction, for each of
659 the 4 stimulus conditions, bootstrapped 100 times over epochs. Arrows indicate the median rate for each condition. (B)
660 Both-hemifield minus blank broadband SNR meshes limited to only those epochs with microsaccades (top row) or
661 without microsaccades (bottom row). Made with *dfdMakeFigure15.m*.

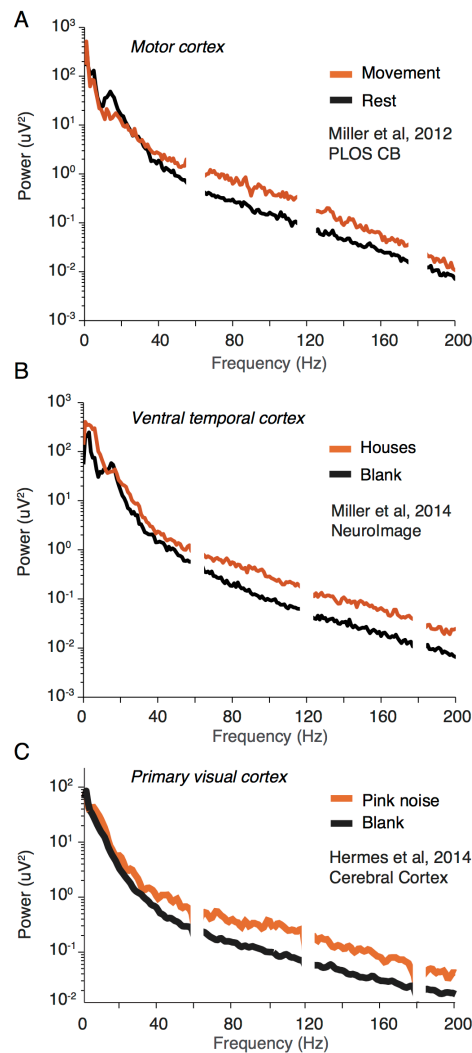
662 Discussion

663 We separated the MEG signal into two components, one time-locked and one asynchronous with
664 the stimulus. The stimulus-locked component was clearly visible in all subjects with minimal
665 preprocessing. The asynchronous signal, spanning 60-150Hz, was visible with little preprocessing
666 in some subjects and the mean across subjects. However, the SNR was low compared to the
667 stimulus-locked component. With our denoising algorithm, SNR more than doubled, resulting in
668 reliable, spatially specific broadband signals in all individuals. We showed in a subset of subjects
669 that the broadband signals could not be explained by systematic biases in the pattern of fixational
670 eye movements, supporting the interpretation that the broadband fields arise from neural activity
671 rather than artifacts associated with eye movements.

672 These results are *qualitatively* consistent with intracranial measurements ([Winawer et al., 2013](#)).
673 However, it has proven difficult to measure extracranial broadband signals arising from neural
674 activity. Below, we discuss the significance of broadband responses, challenges in measuring them
675 extracranially, and the generalizability of our denoising algorithm.

676 Significance of broadband responses

677 A century ago Berger and others described oscillations in surface EEG between 10 and 25Hz
678 ([Berger, 1929](#); [Adrian and Matthews, 1934](#)). More recently, using intracranial recordings, Crone
679 and colleagues ([1998](#)) reported power increases in higher frequencies (75-100Hz) associated with
680 motor movements. Subsequently, this high frequency response was interpreted as a broadband
681 (not oscillatory) signal, thought to reflect increased neuronal activity, rather than increased
682 synchrony ([Miller et al., 2007](#); [Miller et al., 2009c](#)). In support of this interpretation, studies showed
683 that broadband signals correlate with single ([Manning et al., 2009](#)) and multiunit spike rates ([Ray
684 and Maunsell, 2011](#)), and are observed throughout cortex (Figure 16). Under some conditions,
685 broadband is also correlated with the BOLD signal ([Hermes et al., 2012a](#); [Winawer et al., 2013](#)).
686 BOLD signals, however, are influenced by processes other than spiking ([Mathiesen et al., 1998](#);
687 [Logothetis and Wandell, 2004](#); [Sirotin and Das, 2009](#)); hence quantifying broadband responses
688 from the same experimental paradigm studied with fMRI can help disentangle the relative
689 contribution to the observed BOLD response from spiking versus other, non-spiking neural activity.
690 Being able to reliably measure the broadband signal extracranially offers the opportunity to
691 noninvasively measure neuronal spiking activity at a sub-second scale, complementing fMRI and
692 oscillatory and time-locked (evoked) signals commonly measured with MEG and EEG.



693

694 **Figure 16. Broadband signals around the brain.** ECoG studies have measured broadband power elevations associated
695 with perception, movement, language, and cognition (Crone et al., 2006; Miller et al., 2009a; Hermes et al., 2012b; Miller
696 et al., 2014) Examples of broadband field potentials from single ECoG electrodes in motor cortex (top), ventral temporal
697 cortex (middle), and primary visual cortex (bottom). The power increases relative to baseline span at least 50 to 200Hz.
698 Adapted from (A) (Miller et al., 2012); (B) (Miller et al., 2014); (C) (Hermes et al., 2015).

699 Prior measures of extracranial broadband and gamma band responses

700 *Broadband vs. narrowband gamma.* Several groups have distinguished broadband power increases
701 from narrowband gamma oscillations (Henrie and Shapley, 2005; Ray and Maunsell, 2011). Gamma
702 oscillations are observed in visual cortex for some stimuli (e.g., high contrast gratings) (Kayser et
703 al., 2003; Jia et al., 2011), with a peak frequency between 30 and 100Hz and bandwidth of 10-20Hz.
704 The broadband response occurs in many brain areas for many types of stimuli, spanning at least 50-
705 150Hz, and can extend to lower and higher frequencies (Miller et al., 2009c; Winawer et al., 2013).
706 Robust gamma oscillations have been measured extracranially for grating stimuli (Hoogenboom et
707 al., 2006)(Muthukumaraswamy and Singh, 2013). These oscillations differ from the broadband
708 fields reported here, which span a wider frequency range, have lower amplitude, and likely reflect
709 asynchronous neural activity.

710 *Multiple gamma peaks.* Some extracranial studies have reported multiple distinct signals within the
711 gamma band. For example, Wyart and Tallon-Baudry (2008) and Vidal et. al. (2006) measured MEG

712 responses to gratings and bars, respectively. They reported power increases in two bands, from 45-
713 65Hz and 75-120Hz. Both components were interpreted as oscillations arising from synchronous
714 neural activity, and are likely different from the broadband signals reported here.

715 *Group averaged broadband.* Two MEG studies reported increases in high gamma power (60-140Hz)
716 during recall of visual stimuli (Nieuwenhuis et al., 2008; Nieuwenhuis et al., 2012). These studies
717 showed averages across subjects (22 or 24), so that it is not known whether there were reliable
718 responses in individuals.

719 *Motor cortex.* High frequency signals (~65-100Hz) have been shown from motor cortex measured
720 extracranially (Ball et al., 2008; Darvas et al., 2010). This signal was most evident in group-
721 averaged data and some but not all individuals, and within a relatively narrow band (~20-30Hz
722 wide). Ball et al. (2008) noted that better methods for measuring high frequency broadband
723 extracranially would help resolve whether individual differences were due to measurement
724 limitations or the lack of high frequency brain signals in some subjects. Cheyne et al. (2008)
725 measured high gamma (65-80Hz) with MEG over motor cortex in individual subjects, and
726 speculated that these signals reflect cortico-basal ganglia loops, as the basal ganglia is known to
727 produce narrowband oscillations peaked at 70-80Hz.

728 **Challenges in measuring extracranial broadband responses**

729 *Extracranial broadband signal strength is low.* Although having high SNR after denoising, the MEG
730 broadband signal was nonetheless small relative to baseline – about a 13% increase. Using nearly
731 the identical stimulus, the broadband signal measured by ECoG was ~15 times larger (a ~190%
732 increase) (Winawer et al., 2013). The discrepancy was much smaller for the stimulus-locked signal
733 (almost 8-fold increase with MEG vs. 21-fold with ECoG). Why are MEG broadband signals small?
734 First, MEG sensors pool over a large area, so baseline power reflects activity from a large fraction of
735 the brain, whereas visually driven broadband responses likely come from confined regions
736 (Krusienski et al., 2011). In contrast, both baseline and visual responses in ECoG electrodes arise
737 from the same cortical patch. Second, the amplitude depends not only on pooling area, but also
738 phase coherence. If broadband signals arise from incoherent neural activity, and stimulus-locked
739 signals from coherent (synchronous) activity, then the former will grow with the square-root of the
740 number of sources, and the latter with the number of sources. Since MEG pools over much larger
741 populations than ECoG, the ratio of incoherent signal strength (broadband) to coherent (stimulus-
742 locked) will be much lower. This logic is supported by modeling (Linden et al., 2011) and empirical
743 studies with intra- and extracranial measures, which found that the most coherent intracranial
744 signals were best transmitted outside the head (Pfurtscheller and Cooper, 1975; Dalal et al., 2009).

745 *Extracranial measurements contain multiple noise sources.* Because extracranial broadband power is
746 low, noise is a major impediment. In addition to neural noise (Gonen-Yaacovi et al., 2016), fixational
747 eye movements (Yuval-Greenberg et al., 2008), head muscle contraction (Muthukumaraswamy,
748 2013), and environmental perturbations (Hämäläinen et al., 1993) produce noise measured by MEG
749 and EEG sensors. Many of these noise sources are spectrally broad and hence particularly
750 problematic when investigating neural broadband signals.

751 Although spike fields generated from eye movements can be mistaken for broadband neural
752 activity (Yuval-Greenberg and Deouell, 2009), it is unlikely that our spatially-specific broadband
753 measures were substantially contaminated by eye movement artifacts. This was confirmed by
754 analyses of eye movement data, and the fact that middle posterior sensors where we observed
755 broadband are not usually associated with MEG spike field artifacts (Carl et al., 2012). A second eye
756 movement confound, the electromagnetic fields arising from movement of the retina-to-cornea
757 dipole, causes low frequency artifacts (4-20Hz; (Keren et al., 2010)) and therefore is unlikely to
758 have affected our broadband measures (60-150Hz).

759 Head muscles can also cause spectrally broadband contaminants ([Muthukumaraswamy, 2013](#)), as
760 can external noise sources, e.g., nearby electrical equipment. However, these noise sources are
761 unlikely to be confined to occipital sensors and to co-vary with stimulus condition, and hence do
762 not explain our broadband observations. Moreover, it is likely that these noise sources, if present,
763 were included in our noise pool, and hence MEG Denoise would have reduced their effects.

764 **MEG Denoise and other denoising algorithms**

765 MEG Denoise uses PCA on a subset of sensors to remove noise. In principle, it can capture any noise
766 source contributing to the noise pool, including environmental, oculomotor, muscular, and neural.
767 This differs from algorithms designed to remove environmental noise. Hence MEG Denoise is
768 complementary to these methods. We found that the most effective analysis was either MEG
769 Denoise alone, or MEG Denoise following an environmental denoising algorithm. Our algorithm has
770 much in common with ICA denoising ([Vigario, 1997](#)), with some important differences. First, PCA,
771 unlike ICA, ranks components by variance explained. Second, MEG Denoise explicitly identifies
772 noise sensors. These features enable the algorithm to be fully automated, making it easy to denoise
773 at the time scale of individual events (e.g., >1,000 one-second epochs). If the spatial pattern of the
774 PCs vary over time, then deriving the components independently within short epochs is more
775 effective (Figure 11).

776 To use MEG Denoise for other experimental designs, analyses, or scanners, one would need to
777 change some input parameters. In addition to the experimental design matrix and data, required
778 inputs include the experiment-specific functions to summarize the MEG responses. In our
779 experiments, one function computed the stimulus-locked signal and was used to define the noise
780 pool. For most of our analyses, a second function computed the broadband power to evaluate the
781 results. In principle, one could use a single function to define the noise pool and evaluate the data
782 (as we did for denoising the stimulus-locked signal). For other experiments, one might use a
783 function that computes the amplitude or latency of an evoked response, or the power in a limited
784 temporal frequency band, or any measure relevant to the experiment. Alternatively, one could run a
785 separate localizer experiment to identify a pool of potential sensors of interest and a pool of noise
786 sensors, and then manually enter the list of noise sensors to denoise the main experiment. There
787 are several other optional inputs, such as the method to identify the noise pool, the accuracy metric
788 (SNR/R²). Here, we used the defaults for all optional inputs.

789 **Conclusion**

790 Stimulus-driven broadband brain responses can be quantitatively characterized in individual
791 subjects using a non-invasive method. Because we obtain high SNR measures from short
792 experiments, the broadband signal can be used to address a wide range of scientific questions.
793 Access to this signal opens a window for neuroscientists to study signals associated with neuronal
794 spike rates non-invasively at a high temporal resolution in the living human brain.

795 **References**

- 796 Adachi Y, Shimogawara M, Higuchi M, Haruta Y, Ochiai M (2001) Reduction of non-periodic
797 environmental magnetic noise in MEG measurement by continuously adjusted least
798 squares method. *IEEE T Appl Supercon* 11:669-672.
- 799 Adrian ED, Matthews BH (1934) The interpretation of potential waves in the cortex. *J Physiol*
800 81:440-471.
- 801 Ball T, Demandt E, Mutschler I, Neitzel E, Mehring C, Vogt K, Aertsen A, Schulze-Bonhage A
802 (2008) Movement related activity in the high gamma range of the human EEG.
803 *Neuroimage* 41:302-310.
- 804 Berger H (1929) Über Elektroenkephalogramm des Menschen. *European Archives of Psychiatry*
805 *and Clinical Neuroscience* 87:527-570.
- 806 Brainard DH (1997) The Psychophysics Toolbox. *Spat Vis* 10:433-436.
- 807 Buzsaki G, Anastassiou CA, Koch C (2012) The origin of extracellular fields and currents--EEG,
808 ECoG, LFP and spikes. *Nature reviews Neuroscience* 13:407-420.
- 809 Carl C, Acik A, Konig P, Engel AK, Hipp JF (2012) The saccadic spike artifact in MEG.
810 *Neuroimage* 59:1657-1667.
- 811 Cheyne D, Bells S, Ferrari P, Gaetz W, Bostan AC (2008) Self-paced movements induce high-
812 frequency gamma oscillations in primary motor cortex. *Neuroimage* 42:332-342.
- 813 Crone NE, Sinai A, Korzeniewska A (2006) High-frequency gamma oscillations and human
814 brain mapping with electrocorticography. *Neuroimage* 159:275-295.
- 815 Crone NE, Miglioretti DL, Gordon B, Lesser RP (1998) Functional mapping of human
816 sensorimotor cortex with electrocorticographic spectral analysis. II. Event-related
817 synchronization in the gamma band. *Brain* 121 (Pt 12):2301-2315.

- 818 Dalal SS, Baillet S, Adam C, Ducorps A, Schwartz D, Jerbi K, Bertrand O, Garnero L, Martinerie
819 J, Lachaux JP (2009) Simultaneous MEG and intracranial EEG recordings during
820 attentive reading. *Neuroimage* 45:1289-1304.
- 821 Darvas F, Scherer R, Ojemann JG, Rao RP, Miller KJ, Sorensen LB (2010) High gamma
822 mapping using EEG. *Neuroimage* 49:930-938.
- 823 de Cheveigne A, Simon JZ (2007) Denoising based on time-shift PCA. *Journal of neuroscience*
824 *methods* 165:297-305.
- 825 Engbert R (2006) Microsaccades: A microcosm for research on oculomotor control, attention,
826 and visual perception. *Prog Brain Res* 154:177-192.
- 827 Engbert R, Mergenthaler K (2006) Microsaccades are triggered by low retinal image slip. *Proc*
828 *Natl Acad Sci U S A* 103:7192-7197.
- 829 Fries P, Scheeringa R, Oostenveld R (2008) Finding gamma. *Neuron* 58:303-305.
- 830 Gonen-Yaacovi G, Arazi A, Shahar N, Karmon A, Haar S, Meiran N, Dinstein I (2016) Increased
831 ongoing neural variability in ADHD. *Cortex* 81:50-63.
- 832 Hämäläinen M, Hari R, Ilmoniemi RJ, Knuutila J, Lounasmaa OV (1993)
833 Magnetoencephalography—theory, instrumentation, and applications to noninvasive
834 studies of the working human brain. *Reviews of modern Physics* 65:413.
- 835 Harvey BM, Vansteensel MJ, Ferrier CH, Petridou N, Zuiderbaan W, Aarnoutse EJ, Bleichner
836 MG, Dijkerman HC, van Zandvoort MJ, Leijten FS, Ramsey NF, Dumoulin SO (2013)
837 Frequency specific spatial interactions in human electrocorticography: V1 alpha
838 oscillations reflect surround suppression. *Neuroimage* 65:424-432.
- 839 Henrie JA, Shapley R (2005) LFP power spectra in V1 cortex: the graded effect of stimulus
840 contrast. *Journal of neurophysiology* 94:479-490.

- 841 Hermes D, Miller KJ, Wandell BA, Winawer J (2015) Stimulus Dependence of Gamma
842 Oscillations in Human Visual Cortex. *Cerebral cortex* 25:2951-2959.
- 843 Hermes D, Miller KJ, Vansteensel MJ, Aarnoutse EJ, Leijten FS, Ramsey NF (2012a)
844 Neurophysiologic correlates of fMRI in human motor cortex. *Human brain mapping*
845 33:1689-1699.
- 846 Hermes D, Siero JC, Aarnoutse EJ, Leijten FS, Petridou N, Ramsey NF (2012b) Dissociation
847 between neuronal activity in sensorimotor cortex and hand movement revealed as a
848 function of movement rate. *J Neurosci* 32:9736-9744.
- 849 Honey CJ, Thesen T, Donner TH, Silbert LJ, Carlson CE, Devinsky O, Doyle WK, Rubin N,
850 Heeger DJ, Hasson U (2012) Slow cortical dynamics and the accumulation of
851 information over long timescales. *Neuron* 76:423-434.
- 852 Hoogenboom N, Schoffelen JM, Oostenveld R, Parkes LM, Fries P (2006) Localizing human
853 visual gamma-band activity in frequency, time and space. *NeuroImage* 29:764-773.
- 854 Jia X, Smith MA, Kohn A (2011) Stimulus selectivity and spatial coherence of gamma
855 components of the local field potential. *J Neurosci* 31:9390-9403.
- 856 Kay KN, Rokem A, Winawer J, Dougherty RF, Wandell BA (2013) GLMdenoise: a fast,
857 automated technique for denoising task-based fMRI data. *Frontiers in neuroscience*
858 7:247.
- 859 Kayser C, Salazar RF, Konig P (2003) Responses to natural scenes in cat V1. *Journal of*
860 *neurophysiology* 90:1910-1920.
- 861 Keren AS, Yuval-Greenberg S, Deouell LY (2010) Saccadic spike potentials in gamma-band
862 EEG: characterization, detection and suppression. *Neuroimage* 49:2248-2263.
- 863 Krusienski DJ, Grosse-Wentrup M, Galan F, Coyle D, Miller KJ, Forney E, Anderson CW (2011)
864 Critical issues in state-of-the-art brain-computer interface signal processing. *J Neural*
865 *Eng* 8:025002.

- 866 Lima B, Cardoso MM, Sirotin YB, Das A (2014) Stimulus-related neuroimaging in task-engaged
867 subjects is best predicted by concurrent spiking. *J Neurosci* 34:13878-13891.
- 868 Linden H, Tetzlaff T, Potjans TC, Pettersen KH, Grun S, Diesmann M, Einevoll GT (2011)
869 Modeling the spatial reach of the LFP. *Neuron* 72:859-872.
- 870 Liu J, Newsome WT (2006) Local field potential in cortical area MT: stimulus tuning and
871 behavioral correlations. *J Neurosci* 26:7779-7790.
- 872 Logothetis NK, Wandell BA (2004) Interpreting the BOLD signal. *Annu Rev Physiol* 66:735-769.
- 873 Manning JR, Jacobs J, Fried I, Kahana MJ (2009) Broadband shifts in local field potential power
874 spectra are correlated with single-neuron spiking in humans. *J Neurosci* 29:13613-
875 13620.
- 876 Mathiesen C, Caesar K, Akgoren N, Lauritzen M (1998) Modification of activity-dependent
877 increases of cerebral blood flow by excitatory synaptic activity and spikes in rat
878 cerebellar cortex. *J Physiol* 512 (Pt 2):555-566.
- 879 Miller KJ, Weaver KE, Ojemann JG (2009a) Direct electrophysiological measurement of human
880 default network areas. *Proc Natl Acad Sci U S A* 106:12174-12177.
- 881 Miller KJ, Sorensen LB, Ojemann JG, den Nijs M (2009b) Power-law scaling in the brain surface
882 electric potential. *PLoS computational biology* 5:e1000609.
- 883 Miller KJ, Zanos S, Fetz EE, den Nijs M, Ojemann JG (2009c) Decoupling the cortical power
884 spectrum reveals real-time representation of individual finger movements in humans. *J*
885 *Neurosci* 29:3132-3137.
- 886 Miller KJ, Honey CJ, Hermes D, Rao RP, denNijs M, Ojemann JG (2014) Broadband changes in
887 the cortical surface potential track activation of functionally diverse neuronal populations.
888 *Neuroimage* 85 Pt 2:711-720.

- 889 Miller KJ, Leuthardt EC, Schalk G, Rao RP, Anderson NR, Moran DW, Miller JW, Ojemann JG
890 (2007) Spectral changes in cortical surface potentials during motor movement. J
891 Neurosci 27:2424-2432.
- 892 Miller KJ, Hermes D, Honey CJ, Hebb AO, Ramsey NF, Knight RT, Ojemann JG, Fetz EE
893 (2012) Human motor cortical activity is selectively phase-entrained on underlying
894 rhythms. PLoS Comput Biol 8:e1002655.
- 895 Muthukumaraswamy SD (2013) High-frequency brain activity and muscle artifacts in MEG/EEG:
896 a review and recommendations. Front Hum Neurosci 7:138.
- 897 Muthukumaraswamy SD, Singh KD (2013) Visual gamma oscillations: the effects of stimulus
898 type, visual field coverage and stimulus motion on MEG and EEG recordings.
899 Neuroimage 69:223-230.
- 900 Nieuwenhuis IL, Takashima A, Oostenveld R, Fernandez G, Jensen O (2008) Visual areas
901 become less engaged in associative recall following memory stabilization. Neuroimage
902 40:1319-1327.
- 903 Nieuwenhuis IL, Takashima A, Oostenveld R, McNoughton BL, Fernandez G, Jensen O (2012)
904 The neocortical network representing associative memory reorganizes with time in a
905 process engaging the anterior temporal lobe. Cereb Cortex 22:2622-2633.
- 906 Norcia AM, Appelbaum LG, Ales JM, Cottareau BR, Rossion B (2015) The steady-state visual
907 evoked potential in vision research: A review. J Vis 15:4.
- 908 Oostenveld R, Fries P, Maris E, Schoffelen JM (2011) FieldTrip: Open source software for
909 advanced analysis of MEG, EEG, and invasive electrophysiological data. Computational
910 intelligence and neuroscience 2011:156869.
- 911 Pelli DG (1997) The VideoToolbox software for visual psychophysics: transforming numbers into
912 movies. Spat Vis 10:437-442.

- 913 Pfurtscheller G, Cooper R (1975) Frequency dependence of the transmission of the EEG from
914 cortex to scalp. *Electroencephalography and clinical neurophysiology* 38:93-96.
- 915 Podvalny E, Yeagle E, Megevand P, Sarid N, Harel M, Chechik G, Mehta AD, Malach R (2017)
916 Invariant Temporal Dynamics Underlie Perceptual Stability in Human Visual Cortex. *Curr*
917 *Biol* 27:155-165.
- 918 Ray S, Maunsell JH (2011) Different origins of gamma rhythm and high-gamma activity in
919 macaque visual cortex. *PLoS biology* 9:e1000610.
- 920 Schalk G, Leuthardt EC (2011) Brain-computer interfaces using electrocorticographic signals.
921 *IEEE Rev Biomed Eng* 4:140-154.
- 922 Seki K, Nakasato N, Fujita S, Hatanaka K, Kawamura T, Kanno A, Yoshimoto T (1996)
923 Neuromagnetic evidence that the P100 component of the pattern reversal visual evoked
924 response originates in the bottom of the calcarine fissure. *Electroencephalography and*
925 *clinical neurophysiology* 100:436-442.
- 926 Sirotin YB, Das A (2009) Anticipatory haemodynamic signals in sensory cortex not predicted by
927 local neuronal activity. *Nature* 457:475-479.
- 928 Taulu S, Simola J (2006) Spatiotemporal signal space separation method for rejecting nearby
929 interference in MEG measurements. *Phys Med Biol* 51:1759-1768.
- 930 Taulu S, Hari R (2009) Removal of magnetoencephalographic artifacts with temporal signal-
931 space separation: demonstration with single-trial auditory-evoked responses. *Hum Brain*
932 *Mapp* 30:1524-1534.
- 933 Vidal JR, Chaumon M, O'Regan JK, Tallon-Baudry C (2006) Visual grouping and the focusing of
934 attention induce gamma-band oscillations at different frequencies in human
935 magnetoencephalogram signals. *J Cogn Neurosci* 18:1850-1862.
- 936 Vigario RN (1997) Extraction of ocular artefacts from EEG using independent component
937 analysis. *Electroen Clin Neuro* 103:395-404.

- 938 Winawer J, Kay KN, Foster BL, Rauschecker AM, Parvizi J, Wandell BA (2013) Asynchronous
939 broadband signals are the principal source of the BOLD response in human visual
940 cortex. *Curr Biol* 23:1145-1153.
- 941 Wyart V, Tallon-Baudry C (2008) Neural dissociation between visual awareness and spatial
942 attention. *J Neurosci* 28:2667-2679.
- 943 Yuval-Greenberg S, Deouell LY (2009) The broadband-transient induced gamma-band
944 response in scalp EEG reflects the execution of saccades. *Brain Topogr* 22:3-6.
- 945 Yuval-Greenberg S, Deouell LY (2011) Scalp-recorded induced gamma-band responses to
946 auditory stimulation and its correlations with saccadic muscle-activity. *Brain Topogr*
947 24:30-39.
- 948 Yuval-Greenberg S, Tomer O, Keren AS, Nelken I, Deouell LY (2008) Transient induced
949 gamma-band response in EEG as a manifestation of miniature saccades. *Neuron*
950 58:429-441.
- 951